Sources of systematic error in DCEMRI estimation of lowlevel bloodbrain barrier leakage

Received: 18 January 2021 | Revised: 19 March 2021 | Accepted: 16 April 2021

DOI: 10.1002/mrm.28833

FULL PAPER

Magnetic Resonance in Medicine

Sources of systematic error in DCE-MRI estimation of low-level blood-brain barrier leakage

Cameron Manning[1,2] | **Michael Stringer**[1,2] | **Ben Dickie**[3] | **Una Clancy**[1,2] | **Maria C. Valdés Hernandez**[1,2] | **Stewart J. Wiseman**[1,2] | **Daniela Jaime Garcia**[1,2] | **Eleni Sakka**[1,2] | **Walter H. Backes**[4] | **Michael Ingrisch**[5] | **Francesca Chappell**[1,2] | **Fergus Doubal**[1,2] | **Craig Buckley**[6] | **Laura M. Parkes**[3] | **Geoff J. M. Parker**[7] | **Ian Marshall**[1,2,8] | **Joanna M. Wardlaw**[1,2,8] | **Michael J. Thrippleton**[1,2,8]

[1]Centre for Clinical Brain Sciences, University of Edinburgh, Edinburgh, United Kingdom

[2]UK Dementia Research Institute, University of Edinburgh, Edinburgh, United Kingdom

[3]Division of Neuroscience and Experimental Psychology, Faculty of Biology, Medicine and Health, University of Manchester, Manchester Academic Health Science Centre, Manchester, United Kingdom

[4]Department of Radiology & Nuclear Medicine, School for Mental Health & Neuroscience and School for Cardiovascular Diseases, Maastricht University Medical Centre, Maastricht, Netherlands

[5]Department of Radiology, Ludwig-Maximilians-University Hospital Munich, Munich, Germany

[6]Siemens Healthcare Limited, United Kingdom

[7]Centre for Medical Image Computing and Department of Neuroinflammation, UCL, London, United Kingdom

[8]Edinburgh Imaging, University of Edinburgh, Edinburgh, United Kingdom

Correspondence
Michael J. Thrippleton, Centre for Clinical Brain Sciences, University of Edinburgh, The Chancellor's Building, 49 Little France Crescent, Edinburgh EH16 4SB, UK.
Email: m.j.thrippleton@ed.ac.uk

Funding information
Garfield Weston Foundation, Grant/Award Number: TSALECT 2015/04; NHA Research Scotland; Stroke Association, Grant/Award Number: TSALECT 2015/04; UK Dementia Research Institute; Horizon 2020 Framework Programme, Grant/Award Number: PHC-03-15; Fondation Leducq, Grant/Award Number: 16 CVD 05; NHS Lothian Research and Development Office; Alzheimer's Research UK; Mrs Gladys Row Fogo Charitable Trust, Grant/Award Number: BRO-D.FID3668413; Medical Research Council, Grant/Award Number: MR/R01566X/1; Alzheimer's Society; Chief Scientist Office, Grant/Award Number: CAF/18/08

Purpose: Dynamic contrast-enhanced (DCE) -MRI with Patlak model analysis is increasingly used to quantify low-level blood-brain barrier (BBB) leakage in studies of pathophysiology. We aimed to investigate systematic errors due to physiological, experimental, and modeling factors influencing quantification of the permeability-surface area product PS and blood plasma volume v_p, and to propose modifications to reduce the errors so that subtle differences in BBB permeability can be accurately measured.

Methods: Simulations were performed to predict the effects of potential sources of systematic error on conventional PS and v_p quantification: restricted BBB water exchange, reduced cerebral blood flow, arterial input function (AIF) delay and B_1^+ error. The impact of targeted modifications to the acquisition and processing were evaluated, including: assumption of fast versus no BBB water exchange, bolus versus slow injection of contrast agent, exclusion of early data from model fitting and B_1^+ correction. The optimal protocol was applied in a cohort of recent mild ischaemic stroke patients.

Results: Simulation results demonstrated substantial systematic errors due to the factors investigated (absolute PS error $\leq 4.48 \times 10^{-4}$ min^{-1}). However, these were

reduced ($\leq 0.56 \times 10^{-4}$ min^{-1}) by applying modifications to the acquisition and processing pipeline. Processing modifications also had substantial effects on in-vivo normal-appearing white matter *PS* estimation (absolute change $\leq 0.45 \times 10^{-4}$ min^{-1}). **Conclusion:** Measuring subtle BBB leakage with DCE-MRI presents unique challenges and is affected by several confounds that should be considered when acquiring or interpreting such data. The evaluated modifications should improve accuracy in studies of neurodegenerative diseases involving subtle BBB breakdown.

KEYWORDS

blood-brain barrier, DCE-MRI, dementia, gadolinium, small vessel disease

1 | INTRODUCTION

Dynamic contrast-enhanced (DCE-) MRI is a frequently used research technique in assessing breakdown of the blood-brain barrier (BBB) in neurological diseases, including dementias, multiple sclerosis, tumors, and stroke.[1] By measuring signal changes following intravenous injection of a gadolinium-based contrast agent (GBCA), DCE-MRI provides quantitative measurements of GBCA leakage from the brain's blood vessels into the interstitial space as the permeability-surface area product *PS*, together with other physiological properties including the blood plasma volume fraction v_p. DCE-MRI has long been applied to investigate tissues where vascular leakage rates are high, such as high-grade brain tumors. However, the technique is now increasingly used for research into conditions such as cerebral small vessel disease (SVD),[2] Alzheimer disease (AD),[3,4] multiple sclerosis,[5] and aging,[6] where BBB pathology is considered to be significant but the degree of GBCA leakage is nevertheless low.

Despite increasing application of DCE-MRI in this setting, the subtle nature of the leakage and technical limitations of current MRI technology limit the precision and accuracy of BBB leakage estimation. High variability in *PS* measurements mean that large sample sizes are required to detect biological effects, while large inter-site variability hinders multi-center studies and meta-analyses. Improvements in accuracy and precision, therefore, would enable clinical associations, disease progression, and treatment effects to be established more reliably and efficiently. The significant impacts of noise, signal drift, and pharmacokinetic model selection have been previously investigated as summarized in recent reviews, together with recommendations for image acquisition and analysis.[7,8] For example, there is consensus that pharmacokinetic analysis using the Patlak approach is optimal in this regime; previous simulation studies show that its two key assumptions (high cerebral blood flow relative to the BBB leakage rate and negligible backflux of GBCA) are typically met and that good model fits are obtained with minimum free parameters.[9-11]

However, previous reviews have also identified other factors with potential to confound quantification (regardless of the model used to predict GBCA distribution) that have not been quantified in this context. For example, it is standard practice in DCE-MRI studies of neurodegenerative diseases to model longitudinal relaxation in the fast water exchange limit (FXL). This assumption, which requires the differences in longitudinal relaxation rates between the tissue compartments to be much smaller than the inter-compartmental water exchange rates,[12,13] might not be valid for subtle GBCA BBB leakage, particularly during and immediately following injection when the vascular longitudinal relaxation rate is high. Therefore, assuming relaxation rates for vascular and extravascular compartments are distinct may provide more accurate estimates of leakage rates. It is also standard practice to use a bolus injection of GBCA, but although fast injection has benefits over constant infusion,[14] the difficulty of resolving rapid first-pass changes in vascular and tissue GBCA concentrations may introduce additional errors. As a consequence of these and other sources of error, and of divergent approaches to study design, image acquisition, and data analysis, reported values of *PS* (or, equivalently here, the volume transfer constant K^{Trans}) and findings in relation to pathology vary widely between studies and research sites,[7] limiting the adoption of these parameters as surrogate biomarkers of BBB integrity.

In this work, we quantify the impact of experimental and physiological effects on measurements of subtle BBB leakage using a Monte-Carlo simulation approach. We hypothesized that BBB water exchange, cerebral blood flow, arterial input function (AIF) delay, flip angle (FA) mis-calibration, and B_1^+ inhomogeneity would all impact the accuracy of *PS* and v_p estimation in the slow-leakage regime. We further evaluated modifications to the DCE-MRI acquisition and analysis pipelines hypothesized to attenuate these effects, specifically: (i) bolus injection versus slow GBCA injection, (ii) inclusion versus exclusion of first-pass tissue data from the model fitting, (iii) fitting data under the FXL versus no exchange limit (NXL; equivalent to the slow exchange limit SXL) assumption

for exchange across the BBB, and (iv) B_1^+ correction. The impacts of processing modifications were also evaluated in-vivo in a cohort of mild stroke patients with varying degrees of SVD severity, with *PS* and v_p estimated in normal-appearing white matter (NAWM), subcortical gray matter (scGM), and white matter hyperintensities (WMH). We provide an open-source MATLAB application with graphical user interface so that measurement accuracy and precision can be estimated for arbitrary DCE-MRI protocols and modeled physiology. The implications of our findings for planning future studies and for interpreting results are discussed.

2 | METHODS

2.1 | Simulations

DCE-MRI time series were simulated using publically accessible scripts (https://doi.org/10.7488/ds/2997) written in-house using Matlab (Mathworks, Natick MA, USA). Except where specified, the white matter tissue physiological and MR parameters used to simulate data are provided in Table 1. Spoiled gradient echo (SPGR) time series were simulated using the in-vivo protocol described in Section 2.2.1 (repetition time/echo time [TR/TE] = 3.4 ms/1.7 ms, FA = 15°, 3 pre- and 29 post-injection acquisitions with total duration 1268 s). The simulated protocol follows recent consensus recommendations for measurement of subtle BBB leakage.[8]

2.1.1 | Pre-contrast T_1 measurement

T_1 measurement using the variable FA (VFA) method (TR = 5.4 ms, FA = 2°, 5°, 12°) was simulated by generating synthetic signals including additive Gaussian noise, with variance adjusted to achieve a test-retest T_1 error comparable to that reported in the literature for 3T MRI (0.7%).[15] The simulated signal was fitted using a non-linear least squares minimization approach to obtain the measured T_1.

2.1.2 | Simulated DCE-MRI signal-time courses

DCE-MRI simulations were performed using two synthetic AIFs corresponding to bolus injection and slow injection over 2 min (Figure 1). A bolus AIF was generated using a population average function following a similar approach to previous studies,[9,10] while a population average slow-injection AIF was constructed using patient measurements, as described in Section 2.2. Full details are provided in the Supporting Information. A venous vascular input function (VIF), which is frequently used for modeling in-vivo data, was obtained by time-shifting the AIF by 6 s.[16,17]

First, the simulated high-temporal-resolution AIF was convolved with the impulse response function for the 2-compartment exchange Model (2CXM) to generate tissue, capillary plasma, and EES concentration curves as described previously.[5,9,10] This model is defined by four parameters: *PS*, EES volume fraction v_e, blood plasma volume fraction v_p, and blood plasma flow F_p. MRI signal was calculated for steady-state SPGR acquisition; BBB water exchange effects were modeled using the 2-site-1-exchange model (2S1X).[18,19]

Second, signal-time courses were sampled at the required temporal resolution (Δt = 39.6 s) and random Gaussian noise added to achieve a temporal signal-to-fluctuation-noise-ratio (SFNR) of 230 to match the average measured in-vivo value. SFNR was calculated as the ratio of the baseline pre-contrast signal to the root mean square of the residuals for the

TABLE 1 Parameters used to generate DCE-MRI simulations

Parameter	Symbol	Value	Source
Haematocrit	*Hct*	0.42	mean over clinical cohort
EES volume fraction	v_e	0.2	Ref. 45
Native T_1 at 3T (blood/NAWM) (s)	T_{10}	1.90/0.92	Ref. 27
BBB water exchange rate in NAWM (s^{-1})	k_{be}	2.75	Ref. 18
T_1 relaxivity of contrast agent (gadobutrol) at 3T ($mM^{-1}\ s^{-1}$)	r_1	5.0	Ref. 22
Plasma flow in NAWM, equal to CBF(1 − *Hct*) (mL 100 g^{-1} min^{-1})	F_p	11	Ref. 24
Signal-to-fluctuation-noise ratio	SFNR	230	in-vivo data
AIF-to-VIF[a] delay (s)	-	+6	Refs. 16,17
Plasma volume fraction in NAWM	v_p	0.015	Ref. 24

Abbreviation: EES, extravascular extracellular space.

[a]VIF measured in a draining vein.

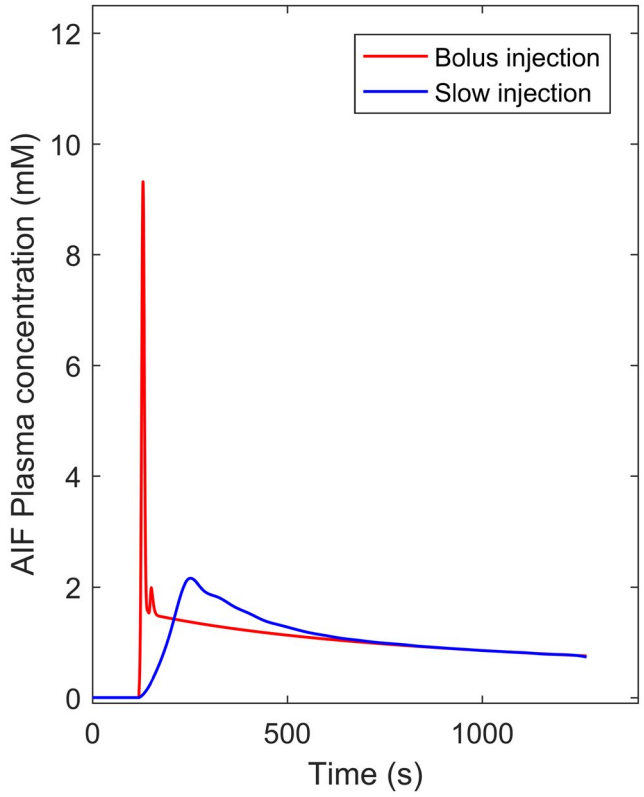

FIGURE 1 Bolus injection AIF (generated with the modified Parker function) and slow injection AIF (based on patient-average measurements) used to generate simulated DCE-MRI data

post-contrast average NAWM signal after fitting to a second order polynomial.[20]

2.1.3 | Simulated measurement of *PS* and v_p

VIF and tissue concentrations were estimated from the simulated MRI signal and T_{10}, assuming the FXL as per standard practice in this application.[10] GBCA concentration was estimated analytically using the equation for the SPGR signal[21] and assuming linear dependence of $1/T_1$ on the concentration ($r_1 = 5.0$ mM^{-1} s^{-1}).[22] Concentration in blood plasma c_p was determined from the blood concentration c_b as $c_p = c_b/(1 - Hct)$, where Hct is the hematocrit. Finally, the Patlak model[23] was fit to tissue concentration-time curves using an unconstrained multiple linear regression approach[8] to yield estimated v_p and PS.

PS and v_p were also estimated assuming the NXL for water exchange across the BBB. A forward model was defined to predict signal enhancement for a given PS and v_p. Pre-contrast compartmental T_{10} was calculated assuming the FXL as described previously,[8] since the rate of water exchange across the BBB is likely to be much greater than the corresponding difference in compartmental R_1.[12,13] GBCA concentrations in the capillary and EES compartments were predicted using the Patlak model, and the corresponding MRI signals were calculated assuming two distinct well-mixed compartments, that is, vascular and extravascular (the combined EES and intracellular compartments) spaces. The two compartmental signals were combined, weighted by their volume fractions, to predict an overall tissue signal. PS and v_p were adjusted to minimize the sum-of-square differences between predicted and "measured" enhancements using the Matlab *lsqcurvefit* function.

All simulations were repeated 1000 times to assess the influence of noise.

2.1.4 | In-silico experiments

Using the simulation framework described in the preceding sections, we assessed the accuracy of PS and v_p measurements in white matter and their sensitivity to variations in physiological and experimental parameters. First, we explored the impact of the BBB water exchange rate, using $k_{be} = 2.75$ s^{-1} as a typical value for healthy NAWM, as well as half of and double this value, to cover potential variation due to age and subtle BBB pathology.[18] Second, we determined the impact of cerebral blood plasma flow rate F_p, using the value 11 mL 100 g^{-1} min^{-1} (equivalent to CBF = 19 mL 100 g^{-1} min^{-1}) representing NAWM in subjects with a similar age range to that of our clinical cohort,[24] and lower values (8.25 and 5.5 mL 100 g^{-1} min^{-1}) to simulate conditions of chronic ischaemia. Third, the effect of AIF delay due to unknown contrast arrival time in the brain circulation (for example due to variations in injection timing, path length and cardiac output) was simulated by repeating simulations with the AIF time-shifted by 0-12 s relative to the reference AIF. For each of these three effects, simulations were performed assuming bolus- and slow-injection protocols, and with and without exclusion of the first 3 data points from the start of the injection (corresponding to a period of 2 min) from the model fitting (specifically, data points were excluded for the purpose of calculating the sum of squares difference between the data and Patlak model prediction, but were always included when calculating the model tissue concentration, which requires integration of the VIF).

Finally, we explored the impact of B_1^+ variation and uncertainty by introducing a proportional error K_{FA} in the transmitted flip angle FA_{true} for both the VFA T_1 and DCE-MRI acquisitions, such that $FA_{true} = FA_{nom} \times K_{FA}$, where FA_{nom} is the nominal FA. Simulations were performed assuming (i) zero FA error, (ii) equal FA error for tissue and the VIF and (iii) unequal FA error for tissue and the VIF. K_{FA} values were obtained from measurements in our clinical cohort using the DESPOT1-HIFI technique, as outlined in section 2.2; values were first averaged over voxels within the VIF and NAWM masks and second over all patients. Simulated data were analyzed assuming the nominal and actual FAs to determine the effect of B_1^+ correction.

2.2 | In-vivo experiments

We used data from the first 50 patients with recent non-disabling ischaemic stroke recruited into an ongoing prospective longitudinal study of cerebral SVDs, as per published protocol.[25] MRI was performed ≥1 month post-stroke to minimize acute effects of stroke on regional BBB integrity. The study was approved by the South-East Scotland Research Ethics Committee (REC 18/SS/0044) and informed written consent was obtained for each participant.

2.2.1 | MRI

Structural imaging, T_1 measurement and DCE-MRI were acquired using a MAGNETOM Prisma 3T clinical MRI scanner (Siemens Healthcare GmbH, Erlangen, Germany) with a 32-channel receive head coil (acquisition parameters are provided as supplementary material of Ref. 25).

Pre-contrast T_1 (T_{10}) maps were measured with voxel-wise correction for (and estimation of) FA error K_{FA}. These were acquired using the DESPOT1-HIFI method[26] (sagittal 3D acquisition, acquisition matrix size $160 \times 200 \times 160$, in-plane acceleration factor 2, 1.2-mm isotropic resolution), consisting of two inversion recovery SPGR sequences (TR = 1040,1940 ms, TE = 1.82 ms, TI = 600,1500 ms, FA = 5°) followed by three SPGR sequences with VFA (TR/TE = 5.4/1.82 ms, FA = 2°,5°,12°). B_1^+-corrected T_1 and K_{FA} parametric maps were derived as described in Ref. 27, while uncorrected (ie, VFA) T_1 was calculated by fitting SPGR images only.

DCE-MRI was acquired using a 3D sagittal T_1w SPGR sequence with non-selective RF excitation and whole-brain coverage (TR/TE = 3.4/1.7 ms, FA = 15°, acquisition matrix size $120 \times 96 \times 96$, 2-mm isotropic resolution). A total of 32 volumes were acquired with a temporal resolution of 39.6 s over 21 min. A dose of 0.1 mmol/kg body weight gadobutrol (1 M Gadovist, Bayer AG, Leverkusen, Germany) was injected intravenously using a power injector following acquisition of three pre-contrast volumes, followed by a 20 mL saline flush; the flow rate was adjusted to deliver the required dose volume over a period of 110-130 s.

Tissue masks representing NAWM, scGM, cerebrospinal fluid, WMHs (a main indicator of SVD), and stroke lesions were derived from structural images, as described in the Supporting Information.

2.2.2 | DCE-MRI processing

DCE-MRI images were spatially realigned (SPM 12 https://www.fil.ion.ucl.ac.uk/spm/) using the brain-extracted (FSL-BET[28]) volumes. A mean pre-contrast image was obtained by averaging the first three volumes and was used as the target image for transforming and resampling the T_{10} maps and binary tissue masks into the DCE-MRI space using FSL FLIRT.[29]

As in previous studies of subtle BBB leakage and consistent with recommendations,[8,30] a venous VIF was used, without scaling or transformation, in order to minimize partial volume, head motion and inflow effects that can affect AIF measurement. The VIF was obtained in each patient by manually selecting five voxels from the superior sagittal sinus, preferentially selecting voxels with a high post-injection signal peak and smooth post-contrast signal decay, and obtaining the mean signal-time course of these voxels. This approach was previously found to have good interobserver reproducibility.[31] The median signal at each time point was obtained from voxels within each tissue mask,[10] in order to suppress the potential impact of skewed intensity distributions and outlier voxels. The signal enhancement was then calculated at each time point relative to the average pre-contrast signal, and concentration was estimated analytically based on the SPGR signal equation and assuming linear dependence of $1/T_1$ on the concentration. PS and v_p were estimated as described in Section 2.1.3 using patient Hct measurements; where no Hct was available from the time of the scan, previous values were obtained from patient records.

2.3 | Statistics

The error in simulated PS and v_p measurements was defined as the difference between the fitted and ground-truth values. The mean and SD of the errors over all runs of the simulation were recorded to indicate the predicted systematic bias and random error, respectively. We defined the sensitivity s of estimated PS or v_p to variation in physiological parameters (ie, k_{be}, F_p and AIF delay) for a given acquisition and processing approach as the range of PS or v_p estimates across all tested values of the confounding parameter, averaged over all simulation runs and simulated values of PS or v_p. s was calculated excluding the notional water exchange cases $k_{be} = 0$ and $k_{be} = 1000\ s^{-1}$. In-vivo measurements were summarized using descriptive statistics and differences were assessed using the paired samples t-test.

3 | RESULTS

3.1 | Simulations

3.1.1 | Water exchange

To determine the impact of BBB water exchange on BBB leakage measurement, DCE-MRI data were simulated for white matter using the 2CXM and 2S1X models to simulate

GBCA and water exchange, respectively (Figure 2). *PS* estimates obtained using the Patlak approach with the standard FXL assumption are substantially overestimated. The systematic error is greater for bolus (3.02-3.83 × 10^{-4} min^{-1}, excluding the notional cases k_{be} = 0, 1000 s^{-1}) versus slow injection (0.84-1.15 × 10^{-4} min^{-1}), dependent on other simulation parameters including injection timing; excluding early data points from the fitting reduces the error in the bolus case (0.07-0.60 × 10^{-4} min^{-1}). Fitting data under the NXL assumption reduces the mean error for both bolus (−0.61 to −0.07 × 10^{-4} min^{-1}) and slow (−0.56 to −0.12 × 10^{-4} min^{-1}) injection protocols. Excluding early data points results in slightly lower sensitivity to the BBB water exchange rate for a bolus (*PS* sensitivity 0.12 × 10^{-4} min^{-1}) vs. slow (0.22 × 10^{-4} min^{-1}) injection analyzed under the FXL assumption. k_{be} sensitivity was higher when data were analyzed under the NXL assumption (0.14 × 10^{-4} min^{-1} and 0.28 × 10^{-4} min^{-1} for bolus and slow injection, respectively). Findings with regard to v_p were qualitatively similar (Supporting Information Figure S1, which is available online).

3.1.2 | Cerebral blood flow

To determine the additional impact of cerebral blood flow on BBB leakage measurement, DCE-MRI data were simulated

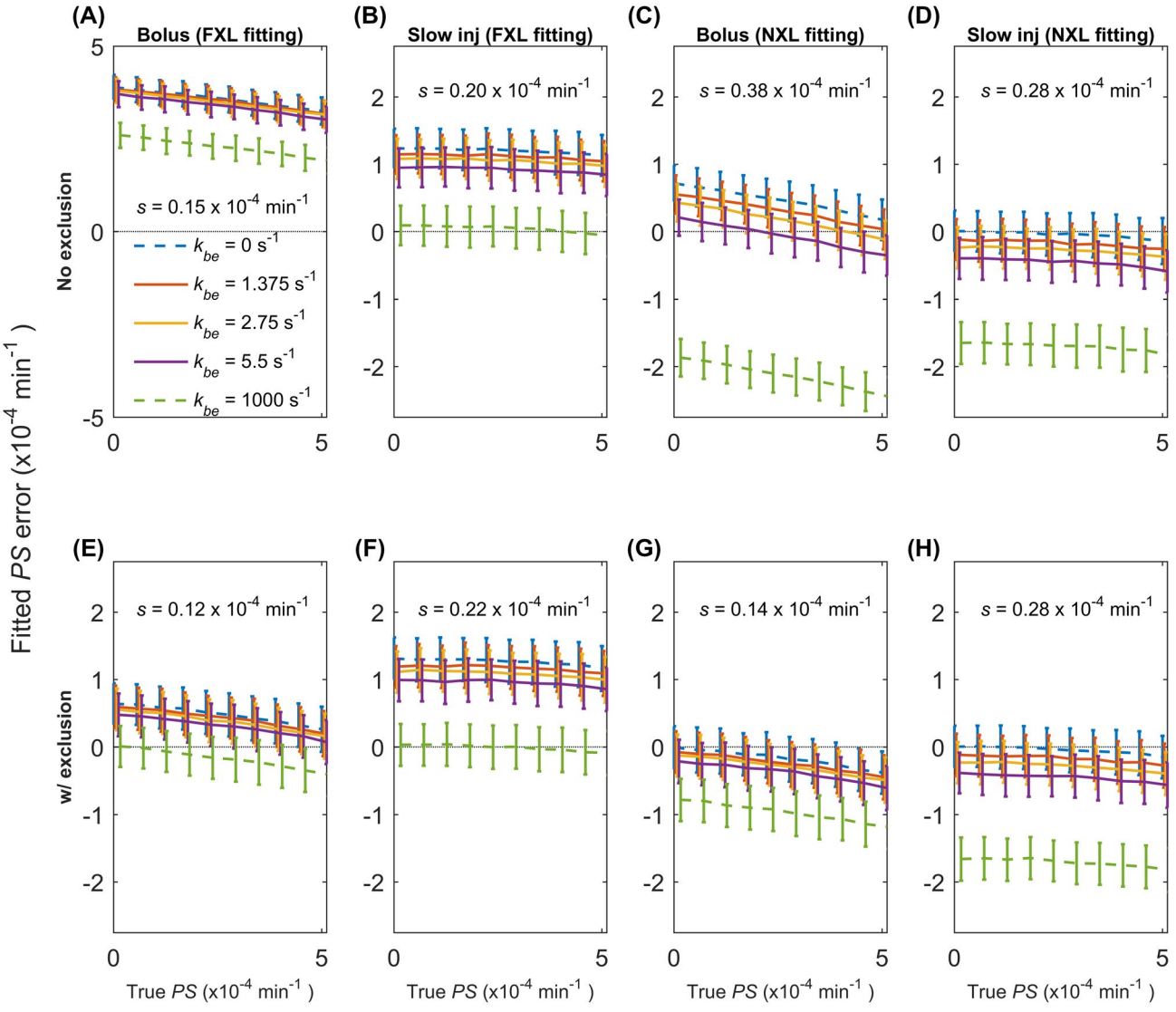

FIGURE 2 Simulation results showing the effect of variable BBB water exchange rate k_{be} on *PS* estimated using the standard Patlak analysis assuming fast water exchange (two left-most columns) and by fitting the same model under the assumption of no BBB water exchange (two right-most columns). Simulations are shown for both bolus and slow injection acquisitions, and with or without exclusion of early data points. Note that a wider y-axis range is used in A. Results are shown for typical (2.75 s^{-1}), low (/2), and high (×2) values of k_{be} in NAWM, as well as notional values representing the no- and fast-exchange limits (k_{be} = 0, 1000 s^{-1}). Error bars show the mean ± SD errors for 1000 simulations; thus, the lines indicate systematic error (bias), while the error bars indicate random error due to noise. Source code to generate this figure is available to download at https://doi.org/10.7488/ds/2997

as described above, assuming different blood plasma flow rates F_p but constant water exchange effects ($k_{be} = 2.75\ s^{-1}$) (Figure 3). *PS* measurements are sensitive to F_p but F_p sensitivity is greater for bolus versus slow injection (0.39 vs. 0.19×10^{-4} min^{-1} for NXL estimation). For both injection protocols, the sensitivity of the fitted parameters to F_p is virtually eliminated by excluding the first three post-injection data points from the cost function (F_p sensitivity $\leq 0.03 \times 10^{-4}$ min^{-1} for NXL estimation). Findings were qualitatively similar using the standard FXL fitting approach and for v_p estimation (Figure S2).

3.1.3 | AIF delay

To determine the additional impact of AIF delay due to variable contrast arrival time in the cerebral arteries, further simulations were performed in the same manner, with a variable time delay (0, 4, 8, and 12 s) applied to the AIF (Figure 4). *PS* measurements are highly sensitive to AIF delay for a bolus injection (delay sensitivity 1.00×10^{-4} min^{-1} for NXL estimation), but this is reduced when early data points are excluded (0.24×10^{-4} min^{-1}). For slow injection *PS* sensitivity is negligible, regardless of whether

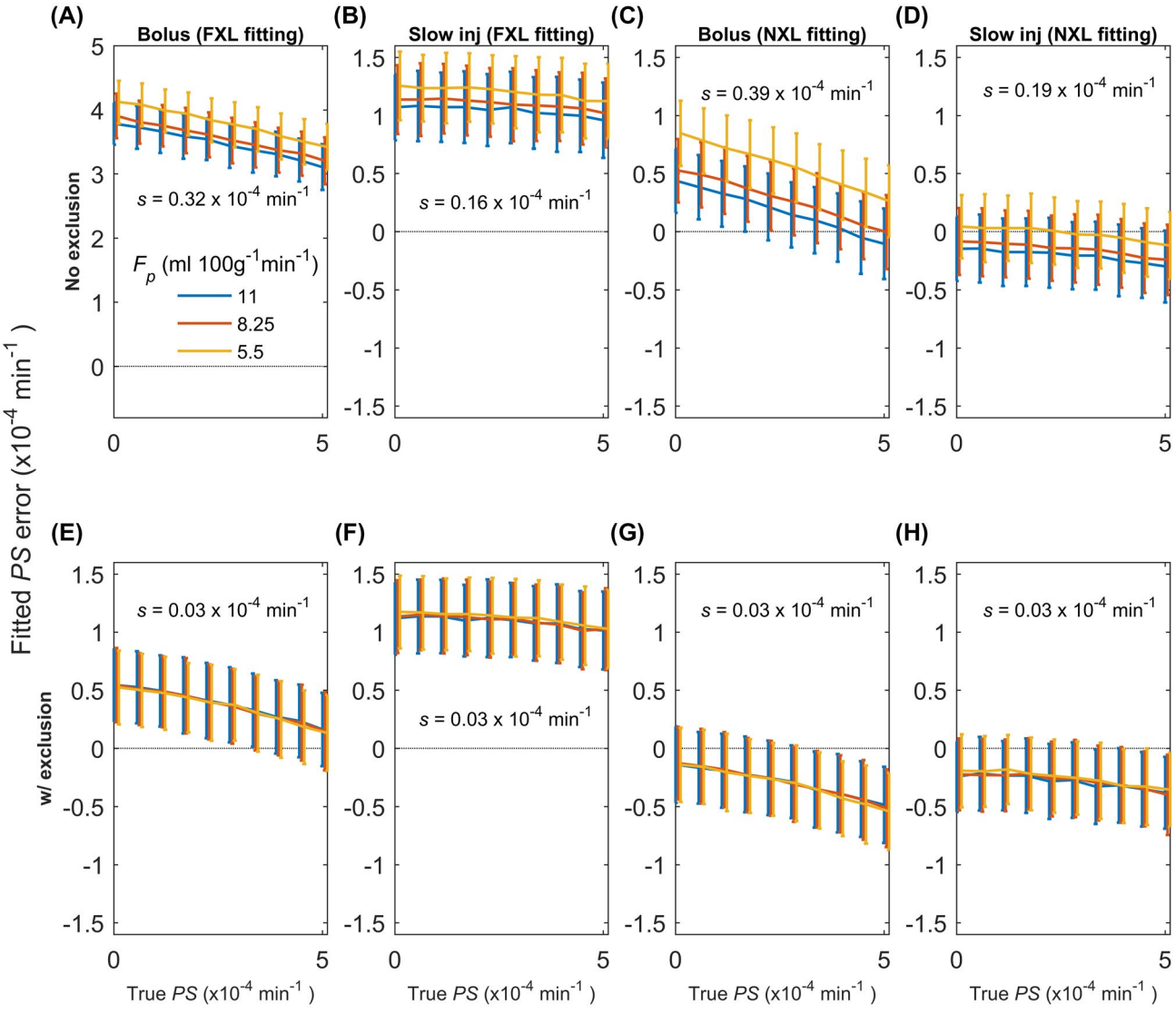

FIGURE 3 Simulation results showing the effects of variable blood plasma flow rate F_p on estimated *PS* incorporating water exchange effects ($k_{be} = 2.75\ s^{-1}$). *PS* was estimated using the standard Patlak approach assuming fast water exchange (two left-most columns) and by fitting the same model under the assumption of no BBB water exchange (two right-most columns). Simulations are shown for both bolus and slow injection acquisitions, and with and without exclusion of early data points. Note that a wider y-axis range is used in A. Results are shown for typical (11 mL 100 g^{-1} min^{-1}), low (−25%), and very low (−50%) values of F_p in NAWM. Error bars show the mean ± SD estimates for 1000 simulations; thus, the lines indicate systematic error (bias) while the error bars indicate random error due to noise. Source code to generate this figure is available to download at https://doi.org/10.7488/ds/2997

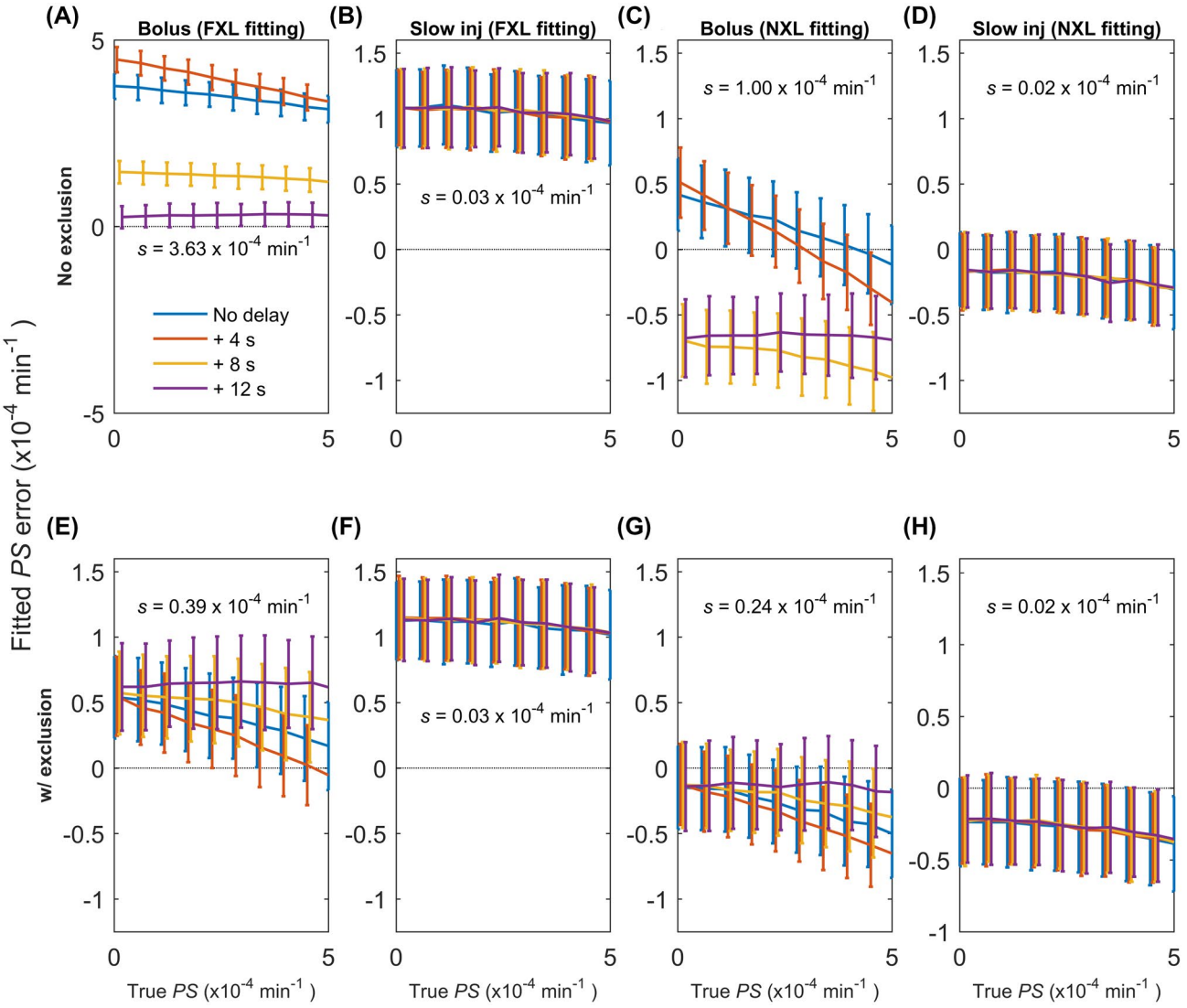

FIGURE 4 Simulation results showing the effects of AIF delay on estimated *PS* incorporating water exchange effects ($k_{be} = 2.75\ s^{-1}$). *PS* was estimated using the standard Patlak approach assuming fast water exchange (two left-most columns), and by fitting the same model under the assumption of no BBB water exchange (two right-most columns). Simulations are shown for both bolus and slow injection acquisitions, and with and without exclusion of early data points. Note that a wider y-axis range is used in A. Results are shown for AIF delays of 0, 4, 8, and 12 s. Error bars show the mean ± SD estimates for 1000 simulations; thus, the lines indicate systematic error (bias), while the error bars indicate random error due to noise. Source code to generate this figure is available to download at https://doi.org/10.7488/ds/2997

early data points are excluded. Findings were qualitatively similar using the standard FXL fitting approach and for v_p estimation (Figure S3).

3.1.4 | B_1^+ inhomogeneity

Further simulations were performed to determine the impact of FA error K_{FA}, assuming typical water exchange effects ($k_{be} = 2.75\ s^{-1}$) and with exclusion of early data points from the model fitting (Figure 5). The impact of spatially uniform FA error is very slight: *PS* estimates are very similar to those obtained with accurate FAs, with low systematic error in *PS* for bolus (-0.47 to -0.11×10^{-4} min^{-1}) and slow (-0.30 to -0.17×10^{-4} min^{-1}) injection acquisitions with NXL fitting. For the more realistic case where B_1^+ inhomogeneity results in different K_{FA} in blood and tissue, the systematic error is substantially greater for both bolus (-1.87 to -0.19×10^{-4} min^{-1}) and slow (-1.90 to -0.38×10^{-4} min^{-1}) injections with NXL fitting. B_1^+ correction results in *PS* estimates close, but not identical, to those obtained in the absence of B_1^+ error. Findings were qualitatively similar using the standard FXL fitting approach and for v_p estimation (Figure S4).

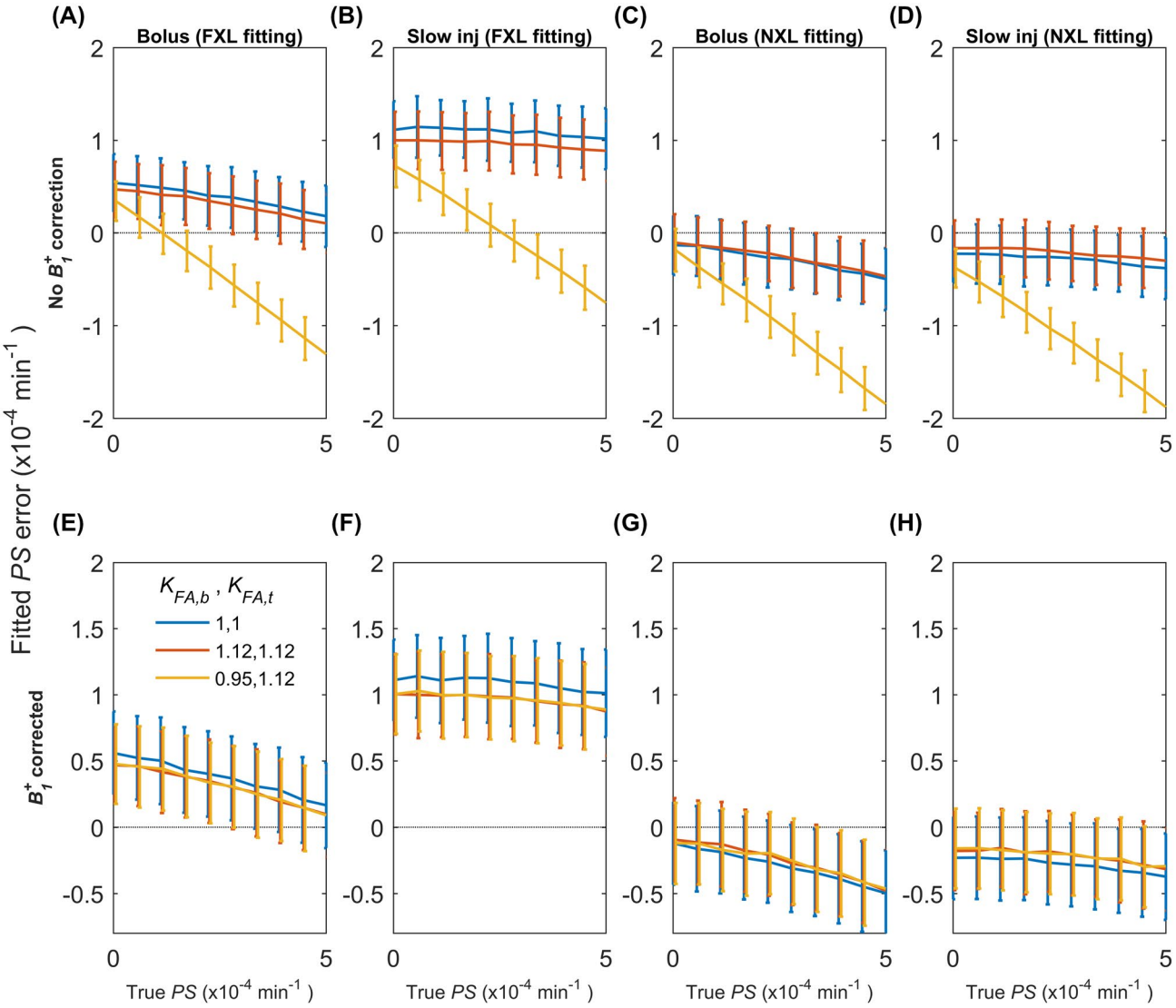

FIGURE 5 Simulation results showing the effects of FA error on estimates of *PS*, incorporating water exchange effects ($k_{be} = 2.75\ s^{-1}$). *PS* was estimated using the standard Patlak approach assuming fast water exchange (two left-most columns), and by fitting the same model under the assumption of no BBB water exchange (two right-most columns); for clarity, results are only shown for analysis with exclusion of early data points. Simulations are shown for both bolus and slow injection acquisitions, and with and without B_1^+ correction. Note each row uses a different y-axis range. Error bars show the mean ± SD estimates for 1000 simulations; thus, the lines indicate systematic error (bias), while the error bars indicate random error due to noise. Source code to generate this figure is available to download at https://doi.org/10.7488/ds/2997

3.2 | In-vivo measurements

After excluding one dataset due to severe motion artefact (N = 1), 49 patients (18 female, age 66.4 ± 9.6 y) had useable DCE-MRI, acquired using the slow-injection protocol described in Section 2.2.1.

We quantified the impact of processing modifications on our in-vivo results (Table 2, Figure 6). There is a substantial negative change in mean *PS* (-0.447×10^{-4} min^{-1} in NAWM) and increase in v_p (+0.17%) estimates when a NXL fitting approach is used in place of the standard FXL method. Excluding early data points from the fitting had less impact, resulting in slightly lower *PS* values (-0.04×10^{-4} min^{-1}) and unchanged v_p. B_1^+ correction had a substantial impact, increasing both *PS* ($+0.201 \times 10^{-4}$ min^{-1}) and v_p (+0.12%) estimates.

Using the processing approach predicted to yield greatest accuracy (NXL fitting, excluding early data points and B_1^+ correction), *PS* values were greater than zero in all tissues ($P < .0077$). *PS* was higher in WMH ($P < .0001$) and scGM ($P < .0001$) vs. NAWM, and v_p was also higher in WMH ($P < .0001$) and scGM ($P < 10^{-5}$) vs. NAWM. There was no significant difference in *PS* between WMH and scGM ($P = .8$), although v_p was higher in scGM vs. WMH ($P < 10^{-5}$).

4 | DISCUSSION AND CONCLUSIONS

In this work, we quantified the impact of biological and instrumental factors on the accuracy of low-level BBB leakage measurements. Simulations predicted clinically significant systematic errors due to injection protocol, restricted water exchange, cerebral blood flow, AIF delay, and B_1^+ inhomogeneity. In some cases, the errors have comparable magnitude to the parameters being measured. Although the recommended

TABLE 2 Mean (SD) of regional *PS* and v_p measured in our clinical cohort (N = 49) and estimated using (i) the standard Patlak approach under the assumption of fast water exchange, (ii) with the assumption of no BBB water exchange (NXL fit), (iii) NXL fit with exclusion of early data points from the cost function, and (iv) NXL fit with exclusion of early data points and B_1^+ correction of T_1 measurement and DCE-MRI

	FXL fit		NXL fit		NXL fit w/exclusion		NXL fit w/ exclusion + B_1^+ correction	
Region	*PS* (10^{-4} min^{-1})	v_p (10^{-2})	*PS* (10^{-4} min^{-1})	v_p (10^{-2})	*PS* (10^{-4} min^{-1})	v_p (10^{-2})	*PS* (10^{-4} min^{-1})	v_p (10^{-2})
NAWM	0.603 (0.576)	0.37 (0.12)	0.156 (0.563)	0.54 (0.14)	0.116 (0.565)	0.54 (0.15)	0.317 (0.798)	0.66 (0.18)
WMH	1.347 (0.997)	0.62 (0.22)	0.542 (0.841)	0.97 (0.33)	0.511 (0.862)	0.98 (0.33)	0.971 (1.309)	1.20 (0.41)
scGM	1.214 (0.820)	0.73 (0.21)	0.290 (0.696)	1.16 (0.25)	0.274 (0.726)	1.16 (0.26)	0.935 (1.209)	1.52 (0.35)

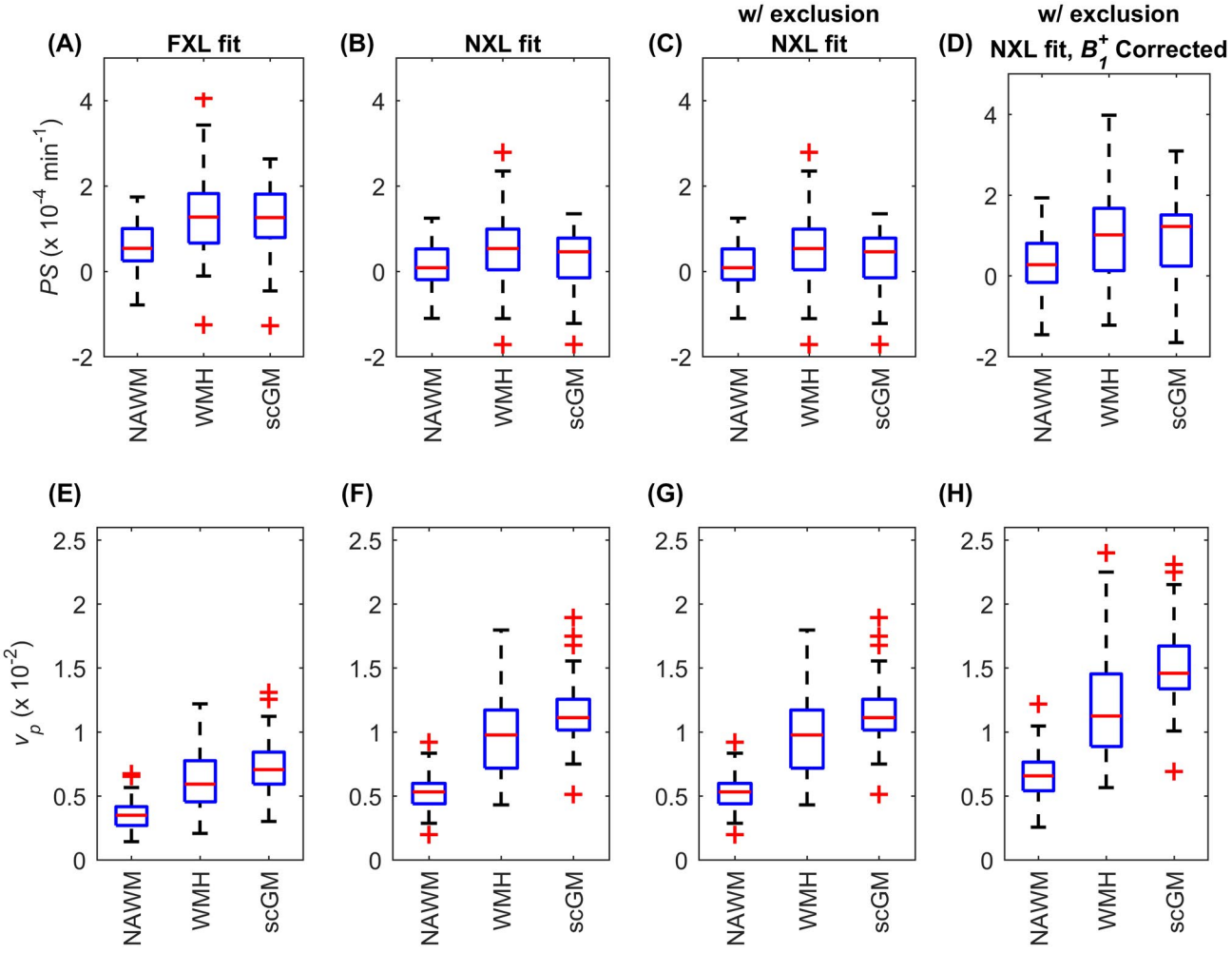

FIGURE 6 *PS* (A-D) and v_p (E-H) measured in our clinical cohort (N = 49) and estimated using (i) the standard Patlak approach under the assumption of fast water exchange (FXL fit), (ii) with the assumption of no BBB water exchange (NXL fit), (iii) NXL fit with exclusion of early data points from the cost function, and (iv) NXL fit with exclusion of early data points and B_1^+ correction of T_1 measurement and DCE-MRI. Whiskers represent the maximum and minimum non-outlier data points. Outliers, shown as red crosses, are defined as >3rd quartile + (1.5 × interquartile range) or <1st quartile − (1.5 × interquartile range)

Patlak analysis method was considered in this work, these confounds are likely to affect subtle BBB leakage measurement using any standard model of GBCA distribution with a comparable MRI protocol. Modifications to the standard acquisition and processing methods were shown to reduce the errors. In-vivo results in minor stroke patients with varying degree of SVD severity reflected previously reported tissue differences; however, parameter estimates changed significantly when the evaluated processing modifications were applied.

4.1 | Causes and reduction of systematic errors

First, we showed that the assumption of fast BBB water exchange, ubiquitous in DCE-MRI studies of neurodegenerative diseases,[8] results in substantial bias in *PS* (up to 4.48×10^{-4} min^{-1}). This is caused by violation of the FXL assumption, with consequent underestimation of GBCA concentration (Figure S5). Since this effect is strongest during the early part of the time course, GBCA concentration appears to increase more rapidly (or decrease more slowly), leading to overestimation of *PS*. The importance of water exchange in contrast-enhanced MRI has long been known,[32] but its impact has not been widely recognised in the BBB literature. Cao et al. reported the effect of restricted water exchange on the GBCA transfer constant, although the impact on accuracy was not presented.[33] Our findings are qualitatively similar to those of Paudyal et al,[12] who simulated measurements of faster BBB leakage with the extended Tofts model. Larsson et al. reported a significant impact on cerebral perfusion values measured using the inversion-recovery SPGR sequence.[34]

We showed that predicted systematic errors are reduced for a bolus injection by excluding early post-injection data points from the model fit, where violation of the FXL is most pronounced. Bias is also substantially reduced by modeling the MRI signal in the NXL. However, *PS* estimates remain somewhat sensitive to the value of k_{be}, which is likely to be altered in neurodegenerative pathology.[18] Variation in individual AIF shape is also likely to affect the bias and requires further investigation. Other approaches could include: acquisition protocols that facilitate simultaneous estimation of k_{be} and *PS*; independent measurement of k_{be} for use in the DCE-MRI signal model; reducing the GBCA dose (at the likely cost of reduced sensitivity to BBB leakage)[35]; and optimizing the acquisition protocol to reduce k_{be} sensitivity.[32,36]

Second, we simulated the impact of cerebral blood flow, which is commonly reduced in aging and neurovascular disease.[37] Previous work has shown that excluding early post-injection time points improves the Patlak model fit, reducing blood flow effects.[10,11] Our simulations results support this approach and, in the case of bolus injection, predict that large systematic *PS* errors and F_p-dependence would otherwise result. Slow-injection DCE-MRI is less sensitive to F_p, since the slower change in arterial GBCA concentration leads to similar arterial, capillary, and venous concentrations (Figure S6), but exclusion of early data points nevertheless reduces F_p sensitivity.

Third, we probed the effect of AIF delay, which can vary in-vivo due to multiple factors including injection timing, cardiac output and path length from the injection site. For a bolus injection, a small delay significantly affects the estimated parameters and a significant error remains even when early data points are excluded, while slow injection of GBCA virtually eliminates the impact. The reason, illustrated in Figure S7, is that the area under the VIF, which approximately determines GBCA extravasation, is more accurately quantified for a slowly changing VIF. For the same reason, additional errors due to variation in bolus shape will likely also be reduced for a slow injection. Furthermore, the high peak concentrations induced by a bolus injection, which may cause T_1 saturation and transverse dephasing, are avoided. This problem of VIF sampling can alternatively be addressed by acquiring data at higher temporal resolution—either during the first-pass[38] or throughout the acquisition—in order to resolve the first-pass profile. However, a compromise must be struck between the temporal resolution, spatial resolution, anatomical coverage and CNR requirements of the application. In this work, we employed a protocol with whole-brain coverage and moderate spatial and temporal resolutions in order to capture pathological changes across multiple brain regions; whole-brain non-selective excitation has the additional benefit of reducing inflow artefact in the large vessels, which can affect VIF quantification. Spatial resolution should nevertheless be adequate to resolve the VIF vessel and the anatomy of interest. A third solution is to substitute a population-averaged VIF during the first-pass period; however, this could lead to errors due to individual variation.

Fourth, we investigated the effect of B_1^+ error. Our results confirm that B_1^+ effects largely self-cancel for the SPGR sequence, as previously reported,[39] provided that the FA error is the same for tissue and VIF. However, our in-vivo measurements using a 3T MRI scanner revealed a 17% difference in average FA for NAWM and VIF. In this case, substantial additional errors in *PS* (around −40%) and v_p were predicted. The reason is illustrated in Figure S8. Fortunately, B_1^+ correction was shown to virtually eliminate this measurement error.

4.2 | In-vivo findings

In our patient cohort, NXL fitting yielded *PS* estimates that were substantially closer to zero in all tissues compared with standard FXL fitting (0.60 vs. 0.16×10^{-4} min^{-1} in NAWM),

while v_p estimates increased by approximately 50%. The incremental effect of excluding early data points was small, as predicted by simulations for the case of a slow injection. B_1^+ correction resulted in higher *PS* and v_p, as predicted; however, final estimates remained lower for *PS* (0.32 vs. 0.60 × 10^{-4} min^{-1} in NAWM) and higher for v_p (0.66 vs. 0.38%) compared with standard FXL analysis without exclusion of early data points or B_1^+ correction. The wider *PS* distribution following B_1^+ correction may represent biological variation, since predicted B_1^+ errors (Figure 5) become more negative as *PS* increases and, therefore, would compress the apparent distribution without B_1^+ correction.

In-vivo data processed with the NXL assumption, exclusion of early data points and B_1^+ correction suggested detectable BBB leakage in all three tissues. Leakage was greater in WMH and scGM compared with NAWM, but similar in WMH and scGM. This pattern of tissue differences confirms the findings of our earlier 1.5T DCE-MRI study in a similar patient cohort.[10] However, *PS* estimates are lower in the present 3T study (0.3 vs. 3.0 × 10^{-4} min^{-1} in NAWM). There are several possible reasons for this. Sham 1.5T DCE-MRI scans without contrast revealed a positive signal drift of approximately 0.08 % min^{-1}, resulting in predicted overestimation of *PS* by around 3.0 × 10^{-4} min^{-1}, while 3T signal drift was close to zero. In addition, 1.5T data were processed using the standard FXL approach, which would likely have resulted in further overestimation. The impact of B_1^+ inhomogeneity, which was not measured at 1.5T, use of different GBCAs and patient differences could also have contributed.

The greater BBB leakage rate measured in WMH versus NAWM in both studies is consistent with BBB dysfunction as a component of WMH pathophysiology, as seen histologically.[40] However, findings from other SVD studies are varied.[8] *PS* is determined by capillary surface area as well as permeability[41]; thus, increased blood volume and potential differences in capillary width[42] could contribute.

v_p was also higher in WMH compared with NAWM, and higher still in scGM. This also confirms our 1.5T findings, however absolute values are somewhat higher in the present study (0.7 vs. 0.6% in NAWM, 1.5 vs. 1.2% in scGM), presumably due to the factors discussed above. Both sets of values are lower than reference values obtained in individuals of similar age using ^{15}O positron emission tomography.[24] This may reflect differences in the cohorts (patients with cerebrovascular disease versus healthy volunteers), resolution and tissue sampling (eroded NAWM masks vs. regions of interest).

4.3 | Implications

Our findings have significant implications for studies of subtle BBB permeability. Inter-site differences in reported *PS* measurements have comparable magnitude[7] to the predicted systematic errors and might be partly caused by the experimental and biological aspects considered in this work, in addition to the previously described impact of scanner drift. Reported differences between and within patients also have a similar magnitude to the predicted systematic errors. For example, Zhang et al. compared SVD patients with controls, reporting a *PS* difference of approximately 0.5 × 10^{-4} min^{-1} [43]; Montagne et al. reported a difference of around 5 × 10^{-4} min^{-1} according to apolipoprotein E status[3] in cognitively normal or early AD participants; finally, Heye et al. reported a difference of 10^{-4} min^{-1} between NAWM and WMH in patients with recent mild stroke.[10] Since variation in BBB water exchange rate, cerebral blood flow, and other factors could potentially mimic or obscure differences in the actual *PS*, their impact should be estimated for specific MRI protocols and, where possible, reduced when designing studies, for example, using the source code provided by the authors.

Some general inferences can also be made. First, it is essential to exclude first-pass data from the model cost function in the case of a bolus injection, in order to avoid large errors due to BBB water exchange, cerebral blood flow rate, and AIF delay. This is not a new recommendation[11] but implementation or otherwise is often not reported in the literature[8] and our simulations reveal the high impact of omitting this measure. Exclusion is less essential in the case of slow injection but nevertheless reduces sensitivity to blood flow.

Second, the substantial systematic errors resulting from the standard FXL assumption can be reduced by modeling the MRI signal in the NXL, with the caveat that *PS* estimates remain somewhat sensitive to the AIF shape and to the water exchange rate.

Third, parameters measured using a bolus injection at low temporal resolution remain moderately sensitive to patient- and protocol-dependent variation in AIF timing, for example due to cardiac output or injection start time. These errors can be eliminated via a slow injection approach. Similar errors are likely to result from variation in bolus shape and arteriovenous delay, which should also be reduced with a slow injection. A disadvantage of this approach is that the full GBCA dose is delivered later; thus, a faster injection rate could be more sensitive to GBCA leakage for shorter acquisitions than simulated here. Further research is needed before recommending an approach, in order to determine the inter-patient variation in VIF profiles, which also modulate the impact of water exchange.

Fourth, FA mapping substantially improves the accuracy of subtle BBB leakage. Failure to correct for variation in the transmitted FA results in substantial errors that vary spatially, could confound tissue comparisons, and that may be larger than those predicted here for the relatively homogeneous B_1^+

field of our dual-transmit 3T MRI system. B_1^+ shimming, where available, should also improve accuracy.

4.4 | Strengths and limitations

Strengths of our work include the use of a computational approach to determine the impact of factors that cannot be easily measured and controlled in-vivo. We propose remedies that were evaluated theoretically and demonstrated in-vivo. Our source code is made publically available for researchers to determine the impact of these effects in future studies. A limitation of our work is that simulation results were obtained for specific sets of parameters, and would be quantitatively different for other protocols and tissues; however, the protocol evaluated is representative of those reported in the literature and the supplied software permits alternative settings to be explored. All simulations are also limited by the forward model used to generate the signal, since knowledge of all underlying biophysical properties is limited. For clarity, we did not include signal drift in the simulations, since this effect has been addressed previously[9,10] and is scanner-dependent. AIF-VIF delay, but not dispersion, was simulated, since there is limited literature regarding the latter and previous work indicates similar time courses[16,17,44]; dispersion will primarily affect the VIF during the period immediately after injection and is likely to affect quantification in a similar manner to variation in AIF timing (Figure 4). The impact should, therefore, be minimized by excluding early data points or using a slow contrast injection.

5 | CONCLUSIONS

In conclusion, we investigated significant confounds of DCE-MRI subtle BBB leakage measurement and approaches to reduce their impact. Properties such as water exchange and blood flow rates, if correlated with pathology, could mimic or disguise differences in BBB leakage if not addressed. In-vivo results in patients with imaging markers of SVD were consistent with simulations and previous findings. Our work should permit improved measurement of BBB leakage in future studies.

ACKNOWLEDGMENTS

The authors acknowledge MRC (MR/R01566X/1) and Siemens Healthcare for funding an iCASE PhD studentship (CM). This work is also supported by NHS Lothian R&D Office (MJT); UK Dementia Research Institute, which receives its funding from DRI Ltd, funded by the UK MRC, Alzheimer's Society, and Alzheimer's Research UK; Fondation Leducq (16 CVD 05) (MS); European Union Horizon 2020 (PHC-03-15, project No 666881) (MS, FC); Stroke Association (UC); Chief Scientist Office of Scotland (CAF/18/08) (UC); Row Fogo Centre for Research into Ageing and the Brain (BRO-D.FID3668413) (MVH, FC); Stroke Association Garfield Weston Foundation Senior Clinical Lectureship (TSALECT 2015/04) (FND); NHA Research Scotland (FND). The authors thank the participants and radiographers at the University of Edinburgh.

DATA AVAILABILITY STATEMENT

Simulation results were generated using publically accessible MATLAB code, available from the Edinburgh DataShare repository: https://doi.org/10.7488/ds/2997.

ORCID

Walter H. Backes https://orcid.org/0000-0001-7905-0681
Francesca Chappell https://orcid.org/0000-0002-7742-1757
Laura M. Parkes https://orcid.org/0000-0001-6488-507X
Michael J. Thrippleton https://orcid.org/0000-0001-7858-9917

REFERENCES

1. Heye AK, Culling RD, Hernandez MDV, Thrippleton MJ, Wardlaw JM. Assessment of blood-brain barrier disruption using dynamic contrast-enhanced MRI. A systematic review. *Neuroimage-Clin*. 2014;6:262-274.
2. Wardlaw JM, Makin SJ, Hernandez MCV, et al. Blood-brain barrier failure as a core mechanism in cerebral small vessel disease and dementia: evidence from a cohort study. *Alzheimers & Dementia*. 2017;13:634-643.
3. Montagne A, Nation DA, Sagare AP, et al. APOE4 leads to blood-brain barrier dysfunction predicting cognitive decline. *Nature*. 2020;581:71-76.
4. van de Haar HJ, Burgmans S, Jansen JF, et al. Blood-brain barrier leakage in patients with early Alzheimer disease. *Radiology*. 2016;281:527-535.
5. Cramer SP, Larsson HB. Accurate determination of blood-brain barrier permeability using dynamic contrast-enhanced T1-weighted MRI: a simulation and in vivo study on healthy subjects and multiple sclerosis patients. *J Cereb Blood Flow Metab*. 2014;34:1655-1665.
6. Verheggen ICM, de Jong JJA, van Boxtel MPJ, et al. Increase in blood-brain barrier leakage in healthy, older adults. *Geroscience*. 2020;42:1183-1193.
7. Raja R, Rosenberg GA, Caprihan A. MRI measurements of blood-brain barrier function in dementia: a review of recent studies. *Neuropharmacology*. 2018;134:259-271.
8. Thrippleton MJ, Backes WH, Sourbron S, et al. Quantifying blood-brain barrier leakage in small vessel disease: review and consensus recommendations. *Alzheimers Dement*. 2019;15:840-858.
9. Barnes SR, Ng TS, Montagne A, Law M, Zlokovic BV, Jacobs RE. Optimal acquisition and modeling parameters for accurate assessment of low Ktrans blood-brain barrier permeability using dynamic contrast-enhanced MRI. *Magn Reson Med*. 2016;75:1967-1977.

10. Heye AK, Thrippleton MJ, Armitage PA, et al. Tracer kinetic modelling for DCE-MRI quantification of subtle blood-brain barrier permeability. *Neuroimage*. 2016;125:446-455.
11. Larsson HB, Courivaud F, Rostrup E, Hansen AE. Measurement of brain perfusion, blood volume, and blood-brain barrier permeability, using dynamic contrast-enhanced T(1)-weighted MRI at 3 tesla. *Magn Reson Med*. 2009;62:1270-1281.
12. Paudyal R, Poptani H, Cai K, Zhou R, Glickson JD. Impact of transvascular and cellular-interstitial water exchange on dynamic contrast-enhanced magnetic resonance imaging estimates of blood to tissue transfer constant and blood plasma volume. *J Magn Reson Imaging*. 2013;37:435-444.
13. Donahue KM, Weisskoff RM, Burstein D. Water diffusion and exchange as they influence contrast enhancement. *J Magn Reson Imaging*. 1997;7:102-110.
14. Tofts PS, Berkowitz BA. Measurement of capillary permeability from the Gd enhancement curve: a comparison of bolus and constant infusion injection methods. *Magn Reson Imaging*. 1994;12:81-91.
15. Lee Y, Callaghan MF, Acosta-Cabronero J, Lutti A, Nagy Z. Establishing intra- and inter-vendor reproducibility of T1 relaxation time measurements with 3T MRI. *Magn Reson Med*. 2019;81:454-465.
16. Sourbron S, Ingrisch M, Siefert A, Reiser M, Herrmann K. Quantification of cerebral blood flow, cerebral blood volume, and blood-brain-barrier leakage with DCE-MRI. *Magn Reson Med*. 2009;62:205-217.
17. Nejad-Davarani SP, Bagher-Ebadian H, Ewing JR, et al. A parametric model of the brain vascular system for estimation of the arterial input function (AIF) at the tissue level. *NMR Biomed*. 2017;30:e3695.
18. Dickie BR, Parker GJ, Parkes LM. Measuring water exchange across the blood-brain barrier using MRI. *Prog Nucl Magn Reson Spectrosc*. 2019;116:19-39.
19. Bains LJ, McGrath DM, Naish JH, et al. Tracer kinetic analysis of dynamic contrast-enhanced MRI and CT bladder cancer data: a preliminary comparison to assess the magnitude of water exchange effects. *Magn Reson Med*. 2010;64:595-603.
20. Friedman L, Glover GH, Fbirn C. Reducing interscanner variability of activation in a multicenter fMRI study: controlling for signal-to-fluctuation-noise-ratio (SFNR) differences. *Neuroimage*. 2006;33:471-481.
21. Elster AD. Gradient-echo MR imaging: techniques and acronyms. *Radiology*. 1993;186:1-8.
22. Rohrer M, Bauer H, Mintorovitch J, Requardt M, Weinmann HJ. Comparison of magnetic properties of MRI contrast media solutions at different magnetic field strengths. *Invest Radiol*. 2005;40:715-724.
23. Patlak CS, Blasberg RG, Fenstermacher JD. Graphical evaluation of blood-to-brain transfer constants from multiple-time uptake data. *J Cereb Blood Flow Metab*. 1983;3:1-7.
24. Leenders KL, Perani D, Lammertsma AA, et al. Cerebral blood-flow, blood-volume and oxygen utilization—normal values and effect of age. *Brain*. 1990;113:27-47.
25. Clancy U, Garcia DJ, Stringer MS, et al. Rationale and design of a longitudinal study of cerebral small vessel diseases, clinical and imaging outcomes in patients presenting with mild ischaemic stroke: mild stroke study 3. *Eur Stroke J*. 2020;6:81-88.
26. Deoni SC. High-resolution T1 mapping of the brain at 3T with driven equilibrium single pulse observation of T1 with high-speed incorporation of RF field inhomogeneities (DESPOT1-HIFI). *J Magn Reson Imaging*. 2007;26:1106-1111.
27. Thrippleton MJ, Blair GW, Valdes-Hernandez MC, et al. MRI relaxometry for quantitative analysis of USPIO uptake in cerebral small vessel disease. *Int J Mol Sci*. 2019;20:776.
28. Smith SM. Fast robust automated brain extraction. *Hum Brain Mapp*. 2002;17:143-155.
29. Jenkinson M, Bannister P, Brady M, Smith S. Improved optimization for the robust and accurate linear registration and motion correction of brain images. *Neuroimage*. 2002;17:825-841.
30. Keil VC, Madler B, Gieseke J, et al. Effects of arterial input function selection on kinetic parameters in brain dynamic contrast-enhanced MRI. *Magn Reson Imaging*. 2017;40:83-90.
31. Heye AK. *Measurement of Subtle Blood-Brain Barrier Disruption in Cerebral Small Vessel Disease using Dynamic Contrast-Enhanced Magnetic Resonance Imaging* [PhD Thesis]. Edinburgh: University of Edinburgh; 2016.
32. Donahue KM, Weisskoff RM, Chesler DA, et al. Improving MR quantification of regional blood volume with intravascular T1 contrast agents: accuracy, precision, and water exchange. *Magn Reson Med*. 1996;36:858-867.
33. Cao Y, Brown SL, Knight RA, Fenstermacher JD, Ewing JR. Effect of intravascular-to-extravascular water exchange on the determination of blood-to-tissue transfer constant by magnetic resonance imaging. *Magn Reson Med*. 2005;53:282-293.
34. Larsson HB, Rosenbaum S, Fritz-Hansen T. Quantification of the effect of water exchange in dynamic contrast MRI perfusion measurements in the brain and heart. *Magn Reson Med*. 2001;46:272-281.
35. Cheng HLM. T-1 measurement of flowing blood and arterial input function determination for quantitative 3D T-1-weighted DCE-MRI. *J Magn Reson Imaging*. 2007;25:1073-1078.
36. Dickie BR, Vandesquille M, Ulloa J, Boutin H, Parkes LM, Parker GJM. Water-exchange MRI detects subtle blood-brain barrier breakdown in Alzheimer's disease rats. *Neuroimage*. 2019;184:349-358.
37. Shi YL, Thrippleton MJ, Makin SD, et al. Cerebral blood flow in small vessel disease: a systematic review and meta-analysis. *J Cerebr Blood F Met*. 2016;36:1653-1667.
38. Jelescu IO, Leppert IR, Narayanan S, Araujo D, Arnold DL, Pike GB. Dual-temporal resolution dynamic contrast-enhanced MRI protocol for blood-brain barrier permeability measurement in enhancing multiple sclerosis lesions. *J Magn Reson Imaging*. 2011;33:1291-1300.
39. Buckley DL, Parker GJ. T1 estimation using variable flip angle spoiled gradient echo for dynamic contrast-enhanced MRI: arterial input measurement improves accuracy in the presence of B1 error. *Proc Intl Soc Mag Reson Med*. 2004;11:1968.
40. Young VG, Halliday GM, Kril JJ. Neuropathologic correlates of white matter hyperintensities. *Neurology*. 2008;71:804-811.
41. Varatharaj A, Liljeroth M, Darekar A, Larsson HBW, Galea I, Cramer SP. Blood-brain barrier permeability measured using dynamic contrast-enhanced magnetic resonance imaging: a validation study. *J Physiol-London*. 2019;597:699-709.
42. Hase Y, Ding R, Harrison G, et al. White matter capillaries in vascular and neurodegenerative dementias. *Acta Neuropathol Com*. 2019;7. https://doi.org/10.1186/s40478-019-0666-x
43. Zhang CE, Wong SM, van de Haar HJ, et al. Blood-brain barrier leakage is more widespread in patients with cerebral small vessel disease. *Neurology*. 2017;88:426-432.

44. Filice S, Crisi G. Dynamic contrast-enhanced perfusion MRI of high grade brain gliomas obtained with arterial or venous waveform input function. *J Neuroimaging*. 2016;26:124-129.
45. Sykova E, Nicholson C. Diffusion in brain extracellular space. *Physiol Rev*. 2008;88:1277-1340.

SUPPORTING INFORMATION

Additional supporting information may be found online in the Supporting Information section.

FIGURE S1 Simulation results showing the effect of variable BBB water exchange rate k_{be} on v_p estimated using the standard Patlak analysis assuming fast water exchange (2 left-most columns) and by fitting the same model under the assumption of no BBB water exchange (2 right-most columns). Simulations are shown for both bolus and slow injection acquisitions, and with or without exclusion of early data points. Note that a shifted y-axis range is used in A. Results are shown for typical (2.75 s^{-1}), low (/2) and high (×2) values of k_{be} in NAWM, as well as notional values representing the fast- and no-exchange limits (k_{be} = 0, 1000 s^{-1}). Error bars show the mean ± standard deviation errors for 1000 simulations, thus the lines indicate systematic error (bias) while the error bars indicate random error due to noise

FIGURE S2 Simulation results showing the effects of variable blood plasma flow rate F_p on estimated v_p, incorporating water exchange effects (k_{be} = 2.75 s^{-1}). v_p was estimated using the standard Patlak approach assuming fast water exchange (2 left-most columns) and by fitting the same model under the assumption of no BBB water exchange (2 right-most columns). Simulations are shown for both bolus and slow injection acquisitions, and with and without exclusion of early data points. Note that a wider y-axis range is used in A. Results are shown for typical (11 ml 100 g^{-1} min^{-1}), low (−25%) and very low (−50%) values of F_p in NAWM. Error bars show the mean ± standard deviation estimates for 1000 simulations, thus the lines indicate systematic error (bias) while the error bars indicate random error due to noise

FIGURE S3 Simulation results showing the effects of AIF delay on estimated v_p, incorporating water exchange effects (k_{be} = 2.75 s^{-1}). v_p was estimated using the standard Patlak approach assuming fast water exchange (2 left-most columns), and by fitting the same model under the assumption of no BBB water exchange (2 right-most columns). Simulations are shown for both bolus and slow injection acquisitions, and with and without exclusion of early data points. Note that a shifted y-axis range is used in A. Results are shown for AIF delays of 0, 4, 8 and 12 s. Error bars show the mean ± standard deviation estimates for 1000 simulations, thus the lines indicate systematic error (bias) while the error bars indicate random error due to noise

FIGURE S4 Simulation results showing the effects of flip angle error on estimates of v_p, incorporating water exchange effects (k_{be} = 2.75 s^{-1}). v_p was estimated using the standard Patlak approach assuming fast water exchange (2 left-most columns), and by fitting the same model under the assumption of no BBB water exchange (2 right-most columns); for clarity, results are only shown for analysis with exclusion of early data points. Simulations are shown for both bolus and slow injection acquisitions, and with and without B_1^+ correction. Note each row uses a different y-axis range. Error bars show the mean ± standard deviation estimates for 1000 simulations, thus the lines indicate systematic error (bias) while the error bars indicate random error due to noise

FIGURE S5 Tissue concentrations (C_t) when measuring *PS* and v_p using routine Patlak analysis assuming the fast exchange limit (left column) or the slow water exchange Patlak analysis (right column), simulated for both bolus (top row) and slow (bottom row) injection of contrast agent. The results demonstrate that, when fitting according to the assumption of fast compartmental water exchange,tissue concentration C_t is consistently underestimated for both bolus and slow injections, predominantly during the early part of the time course. When fitting the enhancement directly under the assumption of slow BBB water exchange, C_t is only slightly overestimated and more accurate *PS* estimation is obtained. Synthetic data were generated as described in the Methods, using the 2CXM model for GBCA exchange, the 2S1X model for water exchange and with the following parameters: $PS = 2.96 \times 10^{-4}$ min^{-1}, v_p = 0.015, v_e = 0.20, k_{be} = 2.75 s^{-1}, F_p = 11 ml 100 g^{-1} min^{-1}. Error bars show the mean ± standard deviation concentration estimates for 1000 simulations

FIGURE S6 Simulated blood plasma GBCA concentrations corresponding to the arterial input function (AIF), vascular input function (VIF) and tissue capilary blood plasma (c_{cp}). Crosses represent MRI measurements of GBCA blood plasma concentration at limited temporal resolution based on the VIF. Data are shown for normal (left column) and reduced (right column) blood plasma flow, and for bolus (top row) and slow (bottom row) injection of GBCA. The data demonstrate that F_p modulates the difference between arterial and capillary GBCA concentrations, which results in erroneous estimation of the vascular contribution to tissue GBCA concentration. The discrepancy is greatest for a bolus injection and during the first-pass, therefore, accuracy is improved by excluding early data points from the cost function during model fitting and by injecting GBCA slowly. Synthetic data were generated as described in the Methods, using the 2CXM model for GBCA exchange and with the following parameters: $PS = 2.96 \times 10^{-4}$ min^{-1}, v_p = 0.015, v_e = 0.20, F_p = 11 ml 100 g^{-1} min^{-1}. For clarity, data were simulated without noise. VIF dispersion was not simulated since there is limited knowledge regarding AIF-VIF dispersion and previous literature suggests closely similar time courses for the two functions

FIGURE S7 Blood plasma GBCA concentrations corresponding to the arterial input function (AIF) and vascular

input function (VIF). Crosses represent VIF concentrations measured at finite temporal resolution (c_p). Data are simulated assuming 4 (left column) and 12 s (right column) AIF delay, and for bolus (top row) and slow (bottom row) injections of contrast agent. For a 4 s delay, the VIF is sampled close to the peak and the area-under-curve (AUC) is overestimated, resulting in inaccurate pharmacokinetic parameter estimates. For a 12 s delay, the peak is missed and the AUC is underestimated. Since the extravascular term of the Patlak model requires the AUC, a delay-dependent error in the fitted pharmacokinetc parameters result. For slow injection of contrast agent, the VIF and its AUC are faithfully represented at the acquired temporal resolution and the effect of delay time is small. Synthetic data were generated as described in the Methods. For clarity, data were simulated without noise

FIGURE S8 Blood plasma GBCA concentrations (c_p, top row; mean over 1000 simulations), tissue GBCA concentration (C_t, middle row), and relative error in both concentrations (bottom row). Data are simulated without flip angle error (left column), for equal flip angle error (K_{FA}) in VIF and tissue (middle column), and for different flip angle errors in VIF and tissue (right column). For no flip angle error, VIF and tissue GBCA concentrations are estimated accurately. Equal flip angle errors in VIF and tissue results in approximately equal proportional errors in both c_p and C_t, thus parameters derived from fitting the Patlak model are almost unchanged. However, unequal flip angle errors result in different errors in VIF and tissue GBCA concentration, resulting in incorrect pharmacokinetic parameter estimates. Synthetic data were generated as described in the Methods, using the 2CXM model for GBCA exchange and with the following parameters: $PS = 2.96 \times 10^{-4}$ min^{-1}, $v_p = 0.015$, $v_e = 0.20$, $F_p = 11$ ml 100 g^{-1} min^{-1}. For clarity, simulations were performed for a slow-injection of GBCA and assuming fast water exchange behaviour, however findings with respect to flip angle error are similar for a bolus injection and for restricted water exchange

How to cite this article: Manning C, Stringer M, Dickie B, et al. Sources of systematic error in DCE-MRI estimation of low-level blood-brain barrier leakage. *Magn Reson Med*. 2021;00:1–16. https://doi.org/10.1002/mrm.28833